ELSEVIER

Using airglow measurements to observe gravity waves in the Martian atmosphere

Stella M.L. Melo [a,*], O. Chiu [a], A. Garcia-Munoz [c], K. Strong [a], J.C. McConnell [c], T.G. Slanger [d], M.J. Taylor [e], R.P. Lowe [b], I.C. McDade [c], D.L. Huestis [d]

[a] *Department of Physics, University of Toronto, Toronto, Ont., Canada M5S 1A7*
[b] *Department of Physics and Astronomy, The University of Western Ontario, London, Canada*
[c] *Department of Earth and Atmospheric Science and Engineer, York University, Toronto, Canada*
[d] *SRI International, Menlo Park, CA, USA*
[e] *Physics Department, Utah State University, Logan, UT, USA*

Abstract

In this paper, we present the first results of model simulations of the airglow response to gravity waves propagating in the Martian atmosphere. This modeling activity has been done in support of the development of two systems to monitor gravity wave activity in the Martian atmosphere through the measurement of contrast in the images of selected airglow features: a zenith-sky imaging system (MARES-Ground) designed to operate from the ground, and an orbiter-based imaging system (MARES-GWIM). Both systems are also briefly described here as well.
© 2005 COSPAR. Published by Elsevier Ltd. All rights reserved.

Keywords: Mars atmosphere; Planetary exploration; Mars atmospheric dynamics; Gravity wave; Airglow

1. Introduction

Atmospheric gravity waves can be generated in the lower atmosphere by a variety of mechanisms (topography, frontal collapse, convection, etc.). When these waves propagate up into the atmosphere their amplitudes grow with altitude as the background density decreases. Eventually they break, transferring energy and momentum into the middle atmosphere. It is now widely acknowledged that it is important to include vertical momentum transport through gravity waves in general circulation models (GCM) describing the Earth atmosphere, since they can substantially affect its circulation and thermal structure (McLandress, 1998; Lindzen, 1973). GCM can produce a

spectrum of explicitly resolved upward-propagating inertia gravity waves. Those waves interact with the mean flow in a manner consistent with that proposed by Lindzen (1981). However, the simulations produced by GCMs run without additional parameterizations of the main-flow drag are still unrealistically close to the radiative equilibrium state. There are a number of different parameterization schemes to incorporate small-scale gravity waves effects in GCMs and it is clear that observational data are crucial to evaluate how realistic a certain parameterization is (Alexander and Rosenlof, 2003).

Dynamical features in the Martian atmosphere have been identified by several instruments. Images of clouds from the Mariner and Viking spacecraft have revealed the presence of dynamical structures such as lee waves and gravity waves (Pettengill and Ford, 2000). Recently, the Mars Pathfinder Atmospheric Structure Investigation (ASI) retrieved information on Martian atmospheric structure from three science accelerometers that measured the
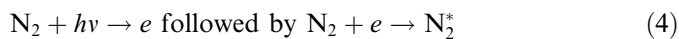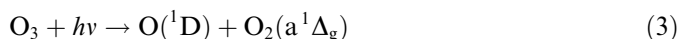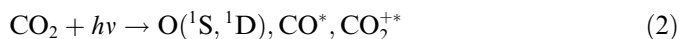
* Corresponding author. Present address: Canadian Space Agency, Saint-Hubert, QC Canada J3Y 8Y9. Tel.: +1 450 926 4947; fax: +1 450 926 4766.
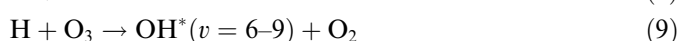*E-mail address:* stella.melo@space.gc.ca (S.M.L. Melo).

deceleration of the probe at all levels in the atmosphere. From the derived temperature profile, wave-like oscillations with an apparent vertical wavelength of ~5 km are evident at altitudes above 60 km (Magalhaes, 1999). The amplitudes of these oscillations show a positive correlation with the background static stability of the atmosphere, consistent with an atmospheric gravity wave interpretation. Also the amplitudes of these oscillations appear to be saturated, suggesting energy and momentum deposition and turbulent mixing.

Many papers have been published studying the dynamical activity of the Mars atmosphere (see for example: Banfield et al., 2003; Forbes et al., 2001; Joshi et al., 1995). Collins et al. (1997) analyzed the effects of inclusion of gravity wave drag in a global circulation model by comparing model initializations with and without gravity wave with temperatures derived from the Mariner 9 IRIS instrument (Santee and Crisp, 1993). They found that without gravity wave drag, the global circulation model temperature field has excessively cold upper level polar regions. Collins et al. (1997) show that in their model, the introduction of gravity wave drag can correct for such cold temperatures by adiabatically warming the atmosphere via a dynamically induced circulation. One thing to consider is that Collins et al. model top is below 80 km altitude and therefore the Hadley circulation cell may not develop properly. Rafkin et al. (2001) has also observed that inclusion of gravity waves in his model leads to improved agreement with measurements. However, existing data lack the spatial and temporal coverage needed to define the full range of gravity wave drag variability and to relate quantitatively possible radiative and mechanical forcing to observed features. One attractive technique that can provide such information is imaging of airglow features.

Airglow, as defined by Chamberlain (1995), is non-thermal atmospheric radiation, excluding aurora and cataclysmic events such as lightning and meteor trails. The main source of energy is the absorption of solar radiation in the UV spectral region. On the dayside, excited states are produced by resonance excitation, photodissociation, and photoelectron impact

$$H + h\nu \rightarrow H^* \tag{1}$$

$$CO_2 + h\nu \rightarrow O(^1S, ^1D), CO^*, CO_2^{+*} \tag{2}$$

$$O_3 + h\nu \rightarrow O(^1D) + O_2(a^1\Delta_g) \tag{3}$$

$$N_2 + h\nu \rightarrow e \text{ followed by } N_2 + e \rightarrow N_2^* \tag{4}$$

The eventual recombination of the resulting ions, electrons, atoms, and unstable molecules produces additional excited states:

$$O_2^+ + e \rightarrow O + O(^1S, ^1D) \tag{5}$$

$$O + O + M \rightarrow O_2^* \tag{6}$$

$$O_2^* + O \rightarrow O(^1S) \tag{7}$$

$$N + O \rightarrow NO^* \tag{8}$$

$$H + O_3 \rightarrow OH^*(v = 6–9) + O_2 \tag{9}$$

A review of the work done on planetary airglows can be found in Slanger and Wolven (2002).

All of these reactions contribute to the day airglow, also called dayglow. The latter group of reactions (5)–(9) also operates throughout the night, producing the night airglow, also called nightglow. Ion–electron recombination reaction (5) occurs mainly in the ionosphere at higher altitudes. The last four chemical recombination reactions (6)–(9) tend to be concentrated in relatively thin vertical layers (called the airglow layer on Earth, generally about 10 km thick) due to the combination of the altitude dependences of the source processes on the top side of the layer and the loss through collisions on the bottom side of the layer.

The spatial and temporal variability of the intensity of nightglow emissions can be used to characterize gravity waves. The primary interaction mechanism is the increase in chemical reaction rates as a gas volume is compressed by the wave. While imaging a single airglow layer from above (or below) allows the horizontal wavelength of the gravity waves to be determined, by imaging simultaneously two (or more) airglow layers at different altitudes the vertical wave number can be recovered, allowing determination of the wave intrinsic frequency and the vertical flux of horizontal momentum, two quantities of immediate relevance to the dynamical effects of gravity waves.

The first observations of airglow activity in the Martian atmosphere were made by ultraviolet spectrometers on Mariners 6, 7, and 9 missions (Barth et al., 1972a,b). Within their 1100–3400 Å band pass, the spectrometers recorded dayglow emissions of H(2s:1216 Å), C(2p3s:1657 Å), O-(2p^{3}3s:1304,1356 Å), O(^{1}S:2972 Å), CO(A$^{\Pi}$, a$^3\Pi \rightarrow$ X$^1\Sigma^+$), and CO$_2^+$(B$^2\Sigma^+$, A$^2\Pi \rightarrow$ X$^2\Sigma^+$). All of these emissions arise from direct photoexcitation or photodissociative excitation high in the Martian atmosphere. Subsequent ground-based telescope observations of the illuminated Martian disc (Noxon et al., 1976) detected emission at 1.27 μm from the O$_2$(a$^1\Delta_g \rightarrow$ X$^3\Sigma_g^-$) Infrared Atmospheric Band, with intensities up to 26 MR (megaRayleigh). This emission results from solar photodissociation of ozone at lower altitudes and can be used as a means for mapping the distribution of ozone in the Martian atmosphere (Novak et al., 2002; Krasnopolsky, 2003), as is also done for the Earth's atmosphere (Mlynczak and Olander, 1995).

Until recently there have been no definitive measurements of the Mars nightglow. Ground-based measurements are particularly difficult because the maximum width of the small dark crescent visible from Earth is only 1.6″, barely more than typical seeing conditions. Even with adaptive optics it will be difficult to reject sunlight scattered from the dayside. The first documented attempt to observe the nightglow of Mars from orbit was made in 1974 by the visible spectrometer on the Mars 5 Orbiter. As reported by Krasnopolsky and Krys'ko (1976), "no emissions exceeding the instrumental threshold of 50 R at 5577 Å were detected". Confidence in this upper bound is limited by the fact that the spectrometer was operational for only a fraction of the mission (less than one orbit) and no infor-

mation was provided that would allow independent estimation of the on-orbit sensitivity. Krasnopolsky and Krys'ko (1976) considered the $O(^1S \rightarrow {}^1D)$ transition at 5577 Å and the OH(8–2) Meinel band near 5900 Å as likely emissions to have been detected. In fact, the 8–2 band is relatively weak in the Earth's atmosphere, with a typical intensity of 60 R (Turnbull and Lowe, 1989). The stronger 6–1 (6497 Å, 120 R), 7–2 (6862 Å, 280 R), and 9–3 (6256 Å, 120 R) bands would also have been within the nominal spectral range of the Mars 5 spectrometer. It is not clear from published information what wavelengths were actually recorded.

Recently, Huestis and Slanger (2002) compared nightglow intensities observed on Earth and Venus with predictions for Mars, including emissions from O, O_2, and OH. Garcia-Munoz et al. (2005) performed a much more detailed study of the predicted intensities of individual Meinel bands, assuming different models for vibrational relaxation. Finally, the first successful nightglow observations in the Mars atmosphere have been reported from the spectroscopy for the investigation of the characteristics of the atmosphere of Mars (SPICAM) instrument on board Mars Express (MEX) orbiter (Bertaux et al., 2005). SPICAM has a spectral coverage from 1180 to 3200 Å. The observed spectrum is very similar with that of Venus over the same wavelength range (Huestis and Slanger, 1993), both being dominated by the $NO(C^2\Pi, A^2\Sigma^+ \rightarrow X^2\Pi)$ bands, but with a slight hint of possible $O(^1S \rightarrow {}^3P)$ emission at 2972 Å. The presence of $O(^1S)$ in the Venus night atmosphere was discovered only recently (Slanger et al., 2001).

In this paper, we use the temperature and constituent concentrations, as well as the airglow chemistry scheme, from Garcia-Munoz et al. (2005) (herein referred as GM), to simulate the airglow response to gravity wave activity in the Martian atmosphere. The focus here is on the OH Meinel bands. Our motivation is to provide support for instrument design and so far, to the best of our knowledge, this is the first study exploring the possibility of using airglow measurements to map gravity wave activity in the atmosphere of Mars. Therefore, we include here only a brief discuss of two instruments proposed to measure the gravity wave activity in the Martial atmosphere: MARES-Ground – which is a ground-based zenith-sky imager designed to measure the temporal evolution of wave-induced radiance fluctuations; and MARES-GWIM – Global Wave Imaging and Mapper for Mars which is an adaptation of GWIM. GWIM is a satellite-borne nadir-viewing imager designed to produce static images of wave-induced radiance fluctuations in two vertically separated night airglow layers in the Earth atmosphere (Lowe et al., 2004).

2. MARS photochemical model

The time-dependent photochemical model of the Martian atmosphere developed by GM is employed here to determine the neutral atmospheric composition and temperature. The model is described in detail in GM and is only briefly discussed here. It solves for the diurnal changes in composition driven by varying insolation between the ground and 80 km altitude. The COSPAR mean Mars temperature profile has been adopted (Seif, 1982) and no temporal variation of temperature as a result of dynamical activities (such as gravity wave, tides, planetary waves, etc.) has been considered. The thermal structure of the atmosphere constrains the water profile throughout most of the lower atmosphere, and in turn, the abundance of odd hydrogen, HO_x (here considered as H, OH, and HO_2), and other active species. K is the so-called eddy diffusion coefficient. In the model K is fixed at $10^6 \text{ cm}^2 \text{ s}^{-1}$ from 0 to 40 km altitude and is assumed to vary exponentially from 10^6 to $10^7 \text{ cm}^2 \text{ s}^{-1}$ between 40 and 80 km altitude. This profile is consistent with the known observational constraints (Korablev, 2002). A simple scheme of precipitation and sublimation of water has been incorporated.

The continuity equations are solved for an atmosphere composed of 13 species: CO_2, CO, O_2, O_3, $O(^3P)$, (O^1D), H_2, H, H_2O (vapor and ice), OH, H_2O_2, and HO_2. The photodissociation rates are evaluated on-line at each time step. No scattering is included in this version of the model. The solar fluxes are averaged to represent mean solar activity (details given in GM). Throughout the lower and middle atmosphere the recycling of OH is governed by the reaction between $O(^3P)$ and HO_2 producing OH and O_2. At altitudes above about 60 km the Nicolet-Bates mechanism, reaction (9), becomes important for the total production of OH. OH* here represents OH in a vibrationally excited state v. The Nicolet-Bates mechanism peaks at night as a result of the greater amount of O_3 present at high altitudes at night. The model values for OH production are similar to those in Nair et al. (1994).

Ozone at daytime is produced by

$$O(^3P) + O_2 + CO_2 \rightarrow O_3 + CO_2 \qquad (10)$$

and lost by photodissociation. At night, in the lower atmosphere O_3 decreases due to the decrease of $O(^3P)$ produced from CO_2 photolysis. However, production continues all day above 50 km altitude leading to a nocturnal increase of O_3 in the middle atmosphere. The resulting O_3 column abundances are comparable with equinox values observed by Clancy et al. (1999). The model results in general are compared with the literature in GM and will not be discussed here.

3. MARS airglow model

As discussed above, here we adopt the same chemical scheme for the OH Meinel airglow as in GM. In brief, for Mars, as for Earth, the hydroxyl nightglow can be assumed to arise from reaction (9). The main non-radiative OH* (herein referred as OH(v) where v represents the vibrational level) loss occurs via quenching with CO_2 and chemical reaction with O, the latter process only being important for the lower vibrational levels. Reaction (9) is the main destruction process for ozone at night in the upper atmosphere. As a

Table 1
Adopted fractional yields, $f(v)$, for the chemical production of OH(v) and the total collisional removal rate coefficient, $k^{CO_2}(v)$

v	$f(v)$	$k^{CO_2}(= \Sigma k^{CO_2}_{v,v'})$ (cm³ s⁻¹)	Reference for k^{CO_2}
1	0	1.8×10^{-13}	Dodd et al. (1991)
2	0	4.8×10^{-13}	Dodd et al. (1991)
3	0	1.4×10^{-12}	Dodd et al. (1991)
4	0.05	2.8×10^{-12}	Dodd et al. (1991)
5	0.05	7.8×10^{-12}	Garcia-Munoz et al. (2005)
6	0.07	2.0×10^{-11}	Garcia-Munoz et al. (2005)
7	0.19	6.7×10^{-11}	Knutsen et al. (1996)
8	0.29	6.4×10^{-11}	Dyer et al. (1997)
9	0.35	5.7×10^{-11}	Chalamala and Copeland (1993)

result, in equilibrium the rate of formation of ozone by reaction (9) must equal the rate of destruction by reaction (10). Hence, the OH(v) emission rate depends only on atomic oxygen concentration, the background atmosphere (for Mars CO_2), and the temperature, T. The dependence on temperature results from the temperature variation of the rate coefficient for reaction (10).

Deactivation of OH(v) proceeds via either radiative relaxation with photon emission

$$OH(v) \rightarrow OH(v') + h\nu \qquad (11)$$

with transition probability $A_{v,v'}$, or by collisional quenching

$$OH(v) + Q \rightarrow OH(v') + Q \qquad (12)$$

with quenching coefficient between the levels (v,v') given by $k^Q(v,v')$ where Q represents the quenching species which can be considered mainly CO_2 for the Martian atmosphere.

Following GM, the relative transition probabilities of Murphy (1971) have been adjusted to the total value $(\Sigma Av,v')$ of Turnbull and Lowe (1989) for each vibrational level. Following the concept introduced by McDade and Llewellyn (1987), two models for collisional deactivation were adopted here: sudden death, when v' is always equal to zero, and collisional cascade when the vibrational deactivation occurs in steps of $\Delta v = 1$. In the sudden death model $k^{CO_2}(v,0) = k^{CO_2}(v)$ and zero otherwise. Hence, the deactivation of one level is not a source for a lower level. In the collisional cascade

model $k^{CO_2}(v, v-1) = v \times k^{CO_2}$ and zero otherwise and each level populates the level just below itself. Although this can be a source of error since multi-quantum collisional deactivation could happen, the lack of measurements makes any other approach seem arbitrary.

Once again, as in GM, $k^{CO_2}(v)$ values from Dodd et al. (1991) are used for $v = 1$–4, from Knutsen et al. (1996) for $v = 7$, Dyer et al., 1997 for $v = 8$, Chalamala and Copeland (1993), for $v = 9$, and an extrapolation with a $\log_{10}(k^{CO_2}) - v$ law for $v = 5$ and 6. The values are given in Table 1. As mentioned in GM, interestingly this relationship assumed seems to represent the entire range $v = 1$–7 reasonably well. As the temperature dependence of the deactivation coefficient remains unknown, we adopted the values as they were measured, i.e., at ambient temperature (about 295 K). This can be an important source of errors since for $v = 10$, Lacoursiere et al. (2003) have reported an increase of nearly 40% when going from temperatures of 300 to 223 K.

As shown in GM, as a result of the lower relative abundance of atomic oxygen in Mars compared to Earth at the altitudes of the emitting OH layer, and to the higher efficiency of CO_2 as an OH(v) quencher, in the Martian atmosphere quenching by atomic oxygen would affect only the lower vibrational levels. Therefore, here quenching by atomic oxygen is assumed to be unimportant.

Assuming chemical equilibrium for the concentration of OH(v), we obtain

$$[OH(v')] = \frac{f_v k_1[H][O_3] + \sum\{A(v,v') + k^{CO_2}(v,v')[CO_2]\}[OH(v)]}{A_T(v') + k^{CO_2}_T(v')[CO_2]}.$$
$$(13)$$

The values of $f(v)$, the fractional yields of the production of OH(v), are taken from Ohoyama et al. (1985) adjusted to the same set of transition probabilities used here. Adopted values for $f(v)$ and $k^{CO_2}_v$ are given in Table 1. The volume emission rate for the Meinel bands is then given by

$$V(v, v') = A(v, v')[OH(v)] \qquad (14)$$

Fig. 1 shows the concentration of OH(v) for selected vibrational levels as a function of altitude calculated using both sudden death and cascade quenching. As discussed in GM, the choice of the quenching model has a major impact
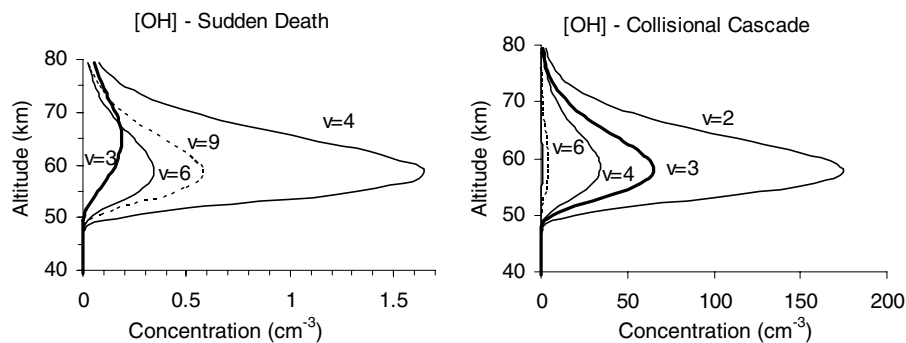

Fig. 1. Model concentrations of OH for selected vibrational levels using the two different assumptions for quenching by CO_2: sudden death (left) and collisional cascade (right).

on the results. As one might expect, the concentrations for the sudden death model are significantly lower than for the collisional cascade model for the lower vibrational levels. The altitude where the concentration peaks, and consequently where the emission peaks, is found to be v-dependent for the sudden death model while almost constant for the collisional cascade model. Such strong differences in concentration, and consequently in emission rate, between the two models results from the relatively high density of the Martian atmosphere ($[CO_2] \sim 4 \times 10^{14}$ cm^{-3} at 60 km) at the OH layer compared to Earth atmosphere ($[O_2] \sim 10^{13}$ cm^{-3} at about 87 km).

As noted above, the only known attempt to measure OH Meinel nightglow in Mars was carried out on the Mars 5 mission, as reported by Krasnopolsky and Krys'ko (1976). Nightglow was not detected and an upper limit of 10^{15} cm^{-6} to the product [H][O$_3$] at 60 km was derived based on the characteristics of the instrumentation used and adopting a photochemical model based on the available parameters. As discussed in GM, the quenching parameters were underestimated and with the more recent deactivation coefficients and transition probabilities, the sudden death upper constraint at 60 km from the limb observation is replaced by $[H][O_3] \leqslant 2 \times 10^{17}$ cm^{-6} and by $[H][O_3] \leqslant 10^{17}$ cm^{-6} if collisional cascade is used. As shown in GM the current photochemical models satisfy these two limits. Therefore, our study indicates that the (8–2) Meinel band would indeed be more strongly quenched than estimated by Krasnopolsky and Krys'ko (1976). However, our results indicate that the lower vibrational bands would be promising candidates for nightglow measurements.

4. Airglow response to gravity wave propagation in Mars

As a first approximation to the problem, we have adapted the Swenson and Gardner (1998) model for the response of the OH airglow emission to perturbations on temperature, atomic oxygen and atmospheric density induced by the propagation of a monochromatic gravity wave, to the Martian atmosphere. The Swenson and Gardner (1998) model is based on the work developed by Gardner and Shelton (1985) and assumes an isothermal and windless atmosphere. Following this approach, the perturbed temperature, oxygen, and atomic oxygen can be given by:

$$\frac{T}{T_u} = \left(\frac{\rho}{\rho_u}\right)^{-1}, \tag{15}$$

$$\frac{[O_2]}{[O_2]_u} = \frac{\rho}{\rho_u}, \tag{16}$$

$$\frac{[CO_2]}{[CO_2]_u} = \frac{\rho}{\rho_u}, \tag{17}$$

$$\frac{[O]}{[O]_u} = \left(\frac{\rho}{\rho_u}\right)^{g_o(z)}, \tag{18}$$

where

$$g_0(z) = \frac{\gamma H - 2sH}{(\gamma - 1)2sH} - \frac{\gamma H}{(\gamma - 1)2sH} \exp\left[-\frac{(z - H_m)}{sH}\right], \tag{19}$$

$$\frac{\rho}{\rho_u} = 1 + \frac{\varepsilon}{(\gamma - 1)} e^{\beta(z - z_{OH})} \cos[\omega t - kx + m(z - z_{OH})]. \tag{20}$$

In these equations T represents temperature, the subscript 'u' represents the undisturbed fields, z is the altitude, z_{OH} is the altitude of the OH airglow peak emission, ω and k are the intrinsic frequency and the vertical wave number, respectively, ε is the wave amplitude at altitude z_{OH}, $1/\beta$ is the amplitude growth length, γ is the ratio of specific heats (assumed here 1.3), s is a shape factor describing the undisturbed OH emission layer assumed as a Gaussian, and H is the scale high ($H = 7.8$ km at 60 km altitude).

Fig. 2 shows the model disturbed T, [CO$_2$], and [O], assuming a wave with $\lambda_z = 20$ km and period of 30 min, together with the respective undisturbed profiles. Figs. 3 and 4 show the response of the bands OH(3–1), OH(6–2), and OH(9–4) to the same monochromatic wave as in Fig. 2 ($\lambda_z = 20$ km and period of 30 min): Fig. 3 shows the time evolution of the altitude profiles. For the OH(9–4) band there is no difference between the two quenching models since here $v = 9$ is assumed as the highest OH vibrational level and is only formed throughout reaction (1). Therefore, only one plot is shown for this emission in Fig. 3. Fig. 4 shows the both percent variation (of undisturbed value) of the column integrated intensities and the column integrated intensities as a function of time.

As expected, the higher OH airglow volume emission rates, and therefore vertical column intensities, occur for the lower vibrational levels, and for the collisional cascade quenching case. As we can see from Fig. 3, the undisturbed OH airglow profiles resulting from the assumption of sudden death quenching are broader than the collisional cascade quenching. Consequently, a wave with $\lambda_z = 20$ km, or smaller, will induce stronger distortions in the shape of the profile for the sudden death case (λ_z comparable to or smaller than the half width of the layer) while for the collisional cascade the same wave will mainly displace the emission layer peak altitude.

Another interesting aspect that can be seen from Fig. 4 is that the v-dependence in the altitude in the peak emission seen in Fig. 1 for the sudden death quenching leads to a phase shift in the vertically integrated intensities. Although we believe a cascading model would be more appropriate for Mars, the phase shift we found using the sudden death model, if confirmed experimentally, could be exploited to determine the vertical wavelength of the propagating gravity wave. It can also provide information on the temperature gradient, if present, in the upper Martian neutral atmosphere. Such information could be directly used to improve the Martian atmospheric models in the aerobreaking altitude region.
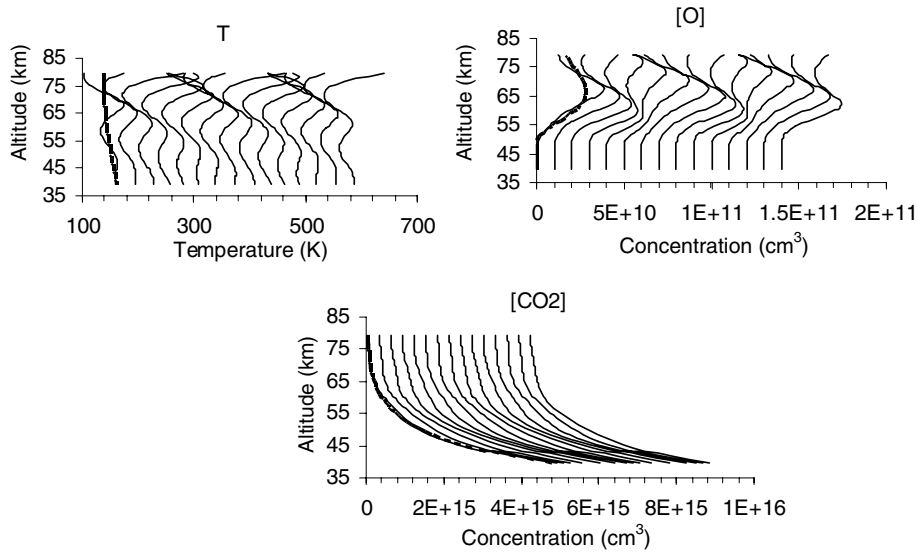
Fig. 2. Disturbed T, [O], and [CO_2], assuming a monochromatic wave with $\lambda_z = 20$ km and period of 30 min. Thick lines represent the undisturbed profiles. The profiles are shifted along the x-axis to simulate time evolution. Therefore, the values expressed in the x-axis correspond only to the undisturbed and the first disturbed profile in the time sequence shown (time steps of 5 min).
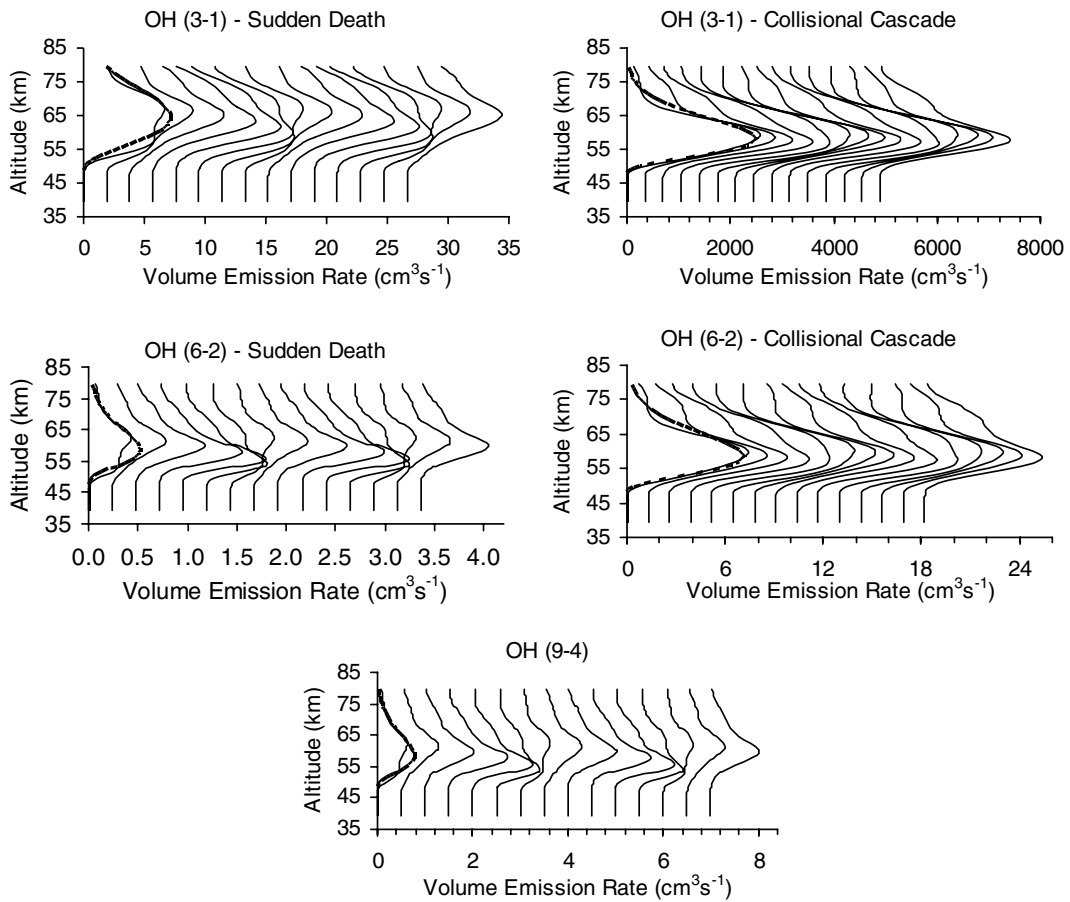

Fig. 3. OH(3–1), OH(6–2), and OH(9–4) airglow band response to the gravity wave activity for the two collisional models: sudden death (left) and collisional cascade (right). The thick line represents the undisturbed profile. Once again, as in Fig. 2, the profiles are shifted along the x-axis to simulate time evolution. Therefore, the values expressed in the x-axis correspond only to the undisturbed and the first disturbed profile in the time sequence shown (time steps of 5 min).
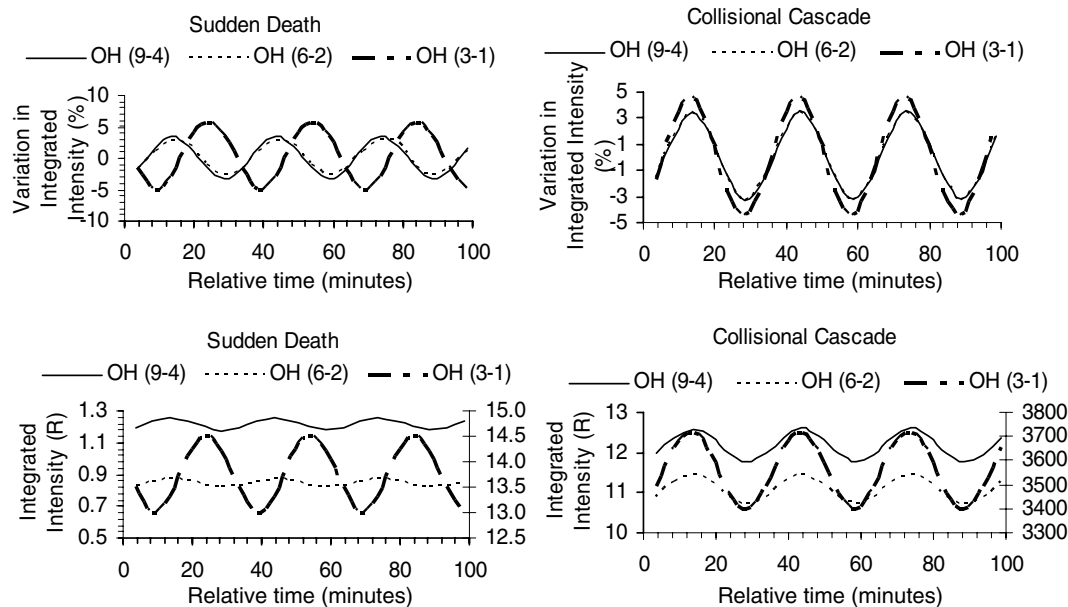
Fig. 4. OH(3–1), OH(6–2), and OH(9–4) airglow band response to the gravity wave activity, as seen in the column integrated intensity, for the two collisional models: sudden death (left) and collisional cascade (right). The upper plots show the time evolution of the variability of each emission relative to the undisturbed value: (disturbed − undisturbed)/undisturbed × 100% while the lower plots show the time evolution of the column integrated intensity in units of rayleigh (1 R = 10^6 photons cm^{-2} s^{-1}). For the lower plots note that the scale for the OH(3–1) band is shown on the right y-axis.

5. Instruments proposed

One of the pioneering studies which showed that images of gravity waves can be obtained from camera images of perturbed terrestrial nightglow emissions was done by Petersen and Kieffaber (1973). Since then, several different ground-based and satellite-based imaging systems have been developed and successfully operated on Earth. Indeed, airglow imaging has proven to be an effective and relatively low cost technique for measuring gravity wave activity, allowing retrieval of parameters such as the wave amplitude, horizontal wavelength, direction of propagation, phase velocity, and wave period (see for example: Hecht et al., 1994; Taylor et al., 1995; Taylor and Bishop, 1995; Swenson and Espy, 1995; Swenson et al., 1995; Mende et al., 1998; Picard et al., 1998). Within the proposed MARES project, Mars Airglow Remote Sensing, we would adapt this approach to Mars. The key objective of MARES is to develop two airglow imagers to operate on the ground and on an orbiter platform to measure gravity wave activity in the Martian atmosphere.

MARES-Ground is a proposed ground-based system intended to operate in a zenith-sky configuration. The instrument concept uses a CCD-based detector (other possibilities are InGaAs and HgCdTe, depending on the spectral range selected), a filter-wheel for wavelength selection and for dark calibration, and the optical system. The wavelength selection would be made through interference filters mounted in the filter wheel, which is a simple, well-developed, and already space-qualified approach. As has been done in Earth, we will measure the temporal evolution and the spatial distribution of the height-integrated intensity of selected airglow emissions. The objective is to build a robust, light-weight, compact, and no-maintenance space-qualified instrument attractive for use on missions to planets that have a solid surface. It has the great advantage that it can be tested, optimized, and cross-calibrated on Earth by operating it side-by-side at a site with an existing airglow imager.

MARES-GWIM is a proposed adaptation of gravity wave imager and mapper (GWIM), a system for an orbiting platform aimed at producing global maps of wave activity. GWIM is in a well-advanced phase of development and is described in detail in Lowe et al. (2004). It consists of four nadir-looking imagers, one each for signal and background for each of the two emissions (one of the OH Meinel bands and the $O_2(b^1\Sigma^+ \rightarrow X^3\Sigma_g^-)$ band). The field of each imager is 175 km cross-track by 80 km along the track. An integration time of about ten seconds is required to achieve the required signal-to-noise ratio. To prevent image smearing due to the effects of satellite motion and the rotation of the earth, GWIM will operate in snapshot mode with an exposure time of about 0.25 second followed by onboard shift-and-add. The total mass is about 10 kg and the power requirement is of the order of 17 W.

The two instruments are independent, but if operated simultaneously would offer the advantage of cross-calibration and cross-validation, two particularly difficult tasks in planetary exploration. Although both instruments have strong heritage, a detailed concept study still needs to be conducted in order to optimize the instrument characteristics.

6. Summary

Mars Pathfinder entry temperature profiles, as well as other observations of the Martian atmosphere, show clear observational evidence of vertically propagating gravity waves. Although existing radiative-convective and general circulation models reproduce the general features of the thermal structures in the lower Martian atmosphere, the observed upper atmospheric temperatures are lower than model predictions. Model simulations suggest that gravity wave drag can account for the cold upper level temperatures in the polar region by adiabatically warming the atmosphere via dynamical-induced circulation. However, the small number of available observations makes it difficult to construct realistic gravity wave parameterization to be inserted in models of the Martian atmosphere. Since the pioneering work done by Petersen and Kieffaber (1973) showing that images of gravity waves can be obtained from camera images of perturbed terrestrial nightglow emissions, several different ground-based and satellite-based imaging systems have been developed and successfully operated on Earth. Because until recently (Bertaux et al., 2005), there were no reported measurements of the nightglow in the Martian atmosphere, the design of airglow imager systems for Mars measurements requires input from modeling simulations in order to select target airglow emissions and then proceed with the design of an appropriate optics and detectors.

In this paper, we used a photochemical model developed by GM, together with a version of the Gardner and Shelton (1985) model adapted to simulate the response of the OH airglow Meinel bands to the propagation of a given gravity wave in the Martian atmosphere. Although this study is limited by the number of assumptions made for the airglow modeling as well as by the approach chosen for the gravity wave modeling, the results suggest that the measurements may be feasible if the OH Meinel bands for lower vibrational levels are chosen as target emissions.

Acknowledgments

References

Alexander, M.J., Rosenlof, K.H. Gravity-wave forcing in the stratosphere: observational constrain from the Upper Atmosphere Research Satellite and implications for parameterization in global models. J. Geophys. Res. 108 (D19), 4597, 2003.

Banfield, D. et al. Forced waves in the Martian atmosphere form MGS TES nadir data. Icarus 161, 319–345, 2003.

Barth, C.A., Hord, C.W., Stewart, A.I., Lane, A.L. Mariner 9 ultraviolet spectrometer experiment: initial results. Science 175, 309–312, 1972a.

Barth, C.A., Stewart, A.I., Hord, C.W., Lane, A.L. Mariner 9 ultraviolet spectrometer experiment: Mars airglow spectroscopy and variations in Lyman alpha. Icarus 17, 457–468, 1972b.

Bertaux, J.-L. et al. Nightglow in the upper atmosphere of Mars and implications for atmospheric transport. Science 307, 566–569, 2005.

Chalamala, B.R., Copeland, R.A. Collision dynamics of $OH(X^2\Pi, v = 9)$. J. Chem. Phys. 99, 5807–5811, 1993.

Chamberlain, J.W. Physics of the Aurora and Airglow. AGU, Washington, DC, 1995.

Clancy, R.T., Wolff, M.J., James, P.B. Minimal aerosol loading and global increases in atmospheric ozone during the 1996–1997 Martian northern spring season. Icarus 138, 49–63, 1999.

Collins, M., Lipson, S.R.J., Blumberg, W.A.M. Formation and vibrational relaxation of $OH(X^2\Pi,v)$ by O_2 and CO_2. Adv. Space Res. 9, 1245–1254, 1997.

Dodd, J.A., Lipson, S.J., Blumberg, W.A.M. Formation and vibrational relaxation of $OH(X^2 s_i,v)$ by O_2 and CO_2. J. Chem. Phys. 95, 5752–5762, 1991.

Dyer, M.J., Knutsen, K., Copeland, R.A. Energy-transfer in the ground-state of OH – measurements of $OH(v = 8, 10, 11)$ removal. J. Chem. Phys. 107, 7809–7815, 1997.

Forbes, J.M., Hagan, M.E., Bougher, S.W., Hollingsworth, J.L. Kelvin wave propagating in the upper atmosphere of Mars and Earth. Adv. Space Sci. 27, 1791–1800, 2001.

Garcia-Munoz, A., McConnell, J.C., McDade, I.C., Melo, S.M.L. Airglow on Mars: some model expectations for the OH Meinel bands and the O_2 IR Atmospheric band. Icarus 176, 75–95, doi:10.1016/j.icarus.2005.01.006, 2005.

Gardner, C.S., Shelton, J.D. Density response of neutral atmospheric layers to gravity wave perturbations. J. Geophys. Res. 90, 1745–1754, 1985.

Hecht, J.H., Walterscheid, R.L., Ross, M.N. 1st Measurements of the 2-dimensional horizontal wave-number spectrum from CCD images of the nightglow. J. Geophys. Res. 99, 11449–11460, 1994.

Huestis, D.L., Slanger, T.G. New perspectives on the Venus nightglow. J. Geophys. Res. 98, 10839–10847, 1993.

Huestis, D.L., Slanger, T.G. The Mars nightglow: inferences from minor species emissions, in: DPS 34th Meeting, Birmingham, AL, October 2002.

Joshi, M.M., Lawrence, B.N., Lewis, S.R. Gravity wave drag in three-dimensional atmospheric models of Mars. J. Geophys. Res. 100, 21235–21246, 1995.

Knutsen, K., Dyer, M.J., Copeland, R.A. Collisional removal of $OH(X^2\Pi, v = 7)$ by O_2, N_2, CO_2, and N_2O. J. Chem. Phys. 104, 5798–5802, 1996.

Korablev, O.I. Solar occultation measurements of the Martian atmosphere on the Phobos spacecraft: water vapor profile, aerosol parameters, and other results. Solar System Res. 36, 15–38, 2002.

Krasnopolsky, V.A. Mapping of Mars O_2 1.27 µm dayglow at four seasonal points. Icarus 165, 315–325, 2003.

Krasnopolsky, V.A., Krys'ko, A.A. On the night airglow of the Martian atmosphere. Space Res. 1, 1005–1008, 1976.

Lacoursiere, J., Dyer, M.J., Copeland, R.A. Temperature dependence of the collisional energy transfer of $OH(v = 10)$ between 220 and 310 K. J. Chem. Phys. 118, 1661–1666, 2003.

Lindzen, R. Wave-mean flow interactions in the upper atmosphere. Bound. Layer Meteor. 4, 327–3243, 1973.

Lindzen, R.S. Turbulence and stress owing to gravity wave and tidal breakdown. J. Geophys. Res. 86, 9707–9714, 1981.

Lowe, R.P., Rowlands, N., Olivery, M. GWIM: a satellite instrument for gravity wave characterization, in: SPIE Europe International Symposium, Maspalomas, Canary Islands, Spain, 2004.

Magalhaes, J.A. Latest results form the Mars Pathfinder atmospheric structure, in: Fifth International Conference in Mars, Passadena, CA, USA, 1999.

McDade, I.C., Llewellyn, E.J. Kinetic parameters related to sources and sinks of vibrationally excited OH in the nightglow. J. Geophys. Res. 92, 7643–7650, 1987.

McLandress, C. On the importance of gravity waves in the middle atmosphere and their parameterization in general circulation models. J. Atmos. Solar-Terr. Phys. 60, 1357–1383, 1998.

Mende, S.B., Frey, H., Geller, S.P., Swenson, G.R. Gravity wave modulated airglow observation from spacecraft. Geophys. Res. Lett. 25, 757–7560, 1998.

Mlynczak, M.G., Olander, D.S. On the utility of the molecular oxygen dayglow emissions as proxies for middle atmospheric ozone. Geophys. Res. Lett. 22, 1377–1380, 1995.

Murphy, R.E. Infrared emission of OH in the fundamental and first overtone bands. J. Chem. Phys. 54, 4852–4859, 1971.

Nair, H. et al. A photochemical model of the Martian atmosphere. Icarus 111, 124–150, 1994.

Novak, R.E., Mumma, M.J., DiSanti, M.A., Russo, N.D., Magee-Sauer, K. Mapping of ozone and water in the atmosphere of Mars near the 1997 aphelion. Icarus 158, 14–23, 2002.

Noxon, J.F., Traub, W.A., Carleton, N.P., Connes, P. Detection of O_2 dayglow emission from Mars and the Mars ozone abundance. Astrophys. J. 207, 1025–1031, 1976.

Ohoyama, H. et al. Initial distribution of vibration of the OH radicals produced in the $H + O_3 \rightarrow OH(X^2\Pi) + O_2$ reaction. Chemiluminescence by a crossed beam technique. Chem. Phys. Lett. 118, 263–267, 1985.

Petersen, A.W., Kieffaber, L.M. Infrared photography of OH airglow structures. Nature 242, 321–322, 1973.

Pettengill, G.H., Ford, P.G. Winter clouds over the north Martian polar cap. Gophys. Res. Lett. 27, 609–612, 2000.

Picard, R.H. et al. Remote sensing of discrete stratospheric gravity-wave structure at 4.3 µm from MSX satellite. Geophys. Res. Lett. 25, 2809–2812, 1998.

Rafkin, S.C.R., Haberle, R., Michaels, T.I. The Mars regional atmospheric modeling system: model description and selected simulations. Icarus 151, 228–256, 2001.

Santee, M., Crisp, D. Thermal structure and dust loading of the Martian atmosphere during late southern summer: Mariner 9 revised. J. Geophys. Res. 98, 3261–3279, 1993.

Seif, A. Post-Viking models for the structure if the summer atmosphere of Mars. Adv. Space Res. 2, 3–17, 1982.

Slanger, T.G., Cosby, P.C., Huestis, D.L., Bida, T.A. Discovery of the atomic oxygen green line in the Venus night airglow. Science 291, 463–465, 2001.

Slanger, T.G., Wolven, B.C. Airglow processes in planetary atmospheres. AGU Monograph 130, 77–93, 2002.

Swenson, G.R., Espy, P.J. Observations of two-dimensional airglow structure and Na density from the ALOHA, October 9, 1993, "Storm Flight". Geophys. Res. Lett. 22, 2845–2848, 1995.

Swenson, G.R., Gardner, C.S. Analytical models for the responses of the mesospheric OH* and Na layers to atmospheric gravity-waves. J. Geophys. Res. 103, 6271–6294, 1998.

Swenson, G.R. et al. ALOHA-93 measurements of intrinsic AGW characteristics using airborne airglow imager and ground-based Na wind/temperature lidar. Geophys. Res. Lett. 22, 2841–2844, 1995.

Taylor, M.J., Bishop, M.B. All-sky measurements of short-period waves imaged in the OI(557.7 nm), Na(589.2 nm) and Near-infrared OH and $O_2(0,1)$ nightglow emissions during the Aloha-93 campaign. Geophys. Res. Lett. 22, 2833–2836, 1995.

Taylor, M.J., Turnbull, D.N., Lowe, R.P. Spectrometric and imaging measurements of a spectacular gravity wave event observed during the ALOHA-93 campaign. Geophys. Res. Lett. 22, 2849–2852, 1995.

Turnbull, D.N., Lowe, R.P. New hydroxyl transition probabilities and their importance in airglow studies. Planet. Space Sci. 37, 723–738, 1989.